

Analysis of Subpulse Generation from Delayed-Interference Signal-Wavelength Converter for Wide Carrier Recovery Rate Range

Jun SAKAGUCHI*, Mads L. NIELSEN^{1†}, Takashi OHIRA[‡], Rei SUZUKI[§], and Yoshiyasu UENO

Department of Electronics Engineering, University of Electro-Communications, 1-5-1 Chofugaoka, Chofu, Tokyo 182-8585, Japan

¹Research Center COM, Technical University of Denmark, Bldg. 345v, DK-2800 Kgs. Lyngby, Denmark

(Received January 11, 2008; accepted April 24, 2008; published online September 12, 2008)

The generation of subpulses in delayed-interference signal-wavelength converters (DISCs) had been suspected as a cause of waveform degradation in their application in ultrafast (~ 160 GHz) optical time division multiplexing (OTDM) communication systems. We reported its first observation in our previous letter. In this paper, after a detailed explanation of our model, experimental method and improved results with respect to those in the previous letter, we discussed the applicability of our model in a wide range of carrier recovery rates in the semiconductor optical amplifier (SOA). Subpulse waveforms were systematically measured for several carrier recovery rates (carrier lifetimes $\tau_{\text{eff}} = 11\text{--}280$ ps), and an increase in subpulse intensity with recovery rate was observed. The calculated intensities showed good agreement with measured data for most recovery rates, which supports our model. Using this model, we numerically showed the trade-off between subpulses and pattern-induced intensity noise, in the same recovery rate range. This trade-off suggests that part of the DISC structure needs improvement. [DOI: 10.1143/JJAP.47.7182]

KEYWORDS: all-optical signal processing, wavelength conversion, delayed-interference signal-wavelength converter (DISC), semiconductor optical amplifier (SOA), nonlinear phase shift, subpulse, pattern-dependent noise

1. Introduction

Several types of all-optical gates based on semiconductor optical amplifiers (SOAs) have been intensively studied,^{1,2)} with the goal of realizing ultrafast, compact, low-power-consumption signal processors for use in future optical time division multiplexing-wavelength division multiplexing (OTDM-WDM) networks and systems. Notably, the delayed-interference signal-wavelength converter (DISC) and its variants have led to some of the most successful achievements in the last decade. 168 Gbps error-free wavelength conversion³⁾ and 40 Gbps error-free ultralong-distance 2R transmission⁴⁾ have been demonstrated using DISCs in their original configuration, and a 320 Gbps wavelength conversion has also been demonstrated using transient cross-phase modulation in the SOA.⁵⁾

It has been noticed, however, that the eye diagram of the DISC output signal often suffers from serious degradation, which could not be ascribed to the well-known pattern-dependent intensity noise. Some modeling research studies^{6,7)} have been focused on explaining this phenomenon, and one fundamental issue has been recognized as the potential source: the generation of small subpulses between return-to-zero-formatted output pulses. We actually observed the generation of subpulses through a gate experiment, and reported it in our former letter.⁸⁾ In addition, we explained the measured characteristics of subpulse waveforms quantitatively using our subpulse generation model. However, we described these issues only partially because of the limited paper length. Furthermore, we reported only a weak generation of subpulses, since the carrier recovery in the SOA had been kept slow throughout the former experiment. It has not been proved, therefore, whether

subpulse generation can be an actual, serious cause of signal degradation.

In this paper, we first report further details of our measurement and theoretical analysis of subpulse generation with improved accuracy using the latest results of SOA-characterization. Then we demonstrate a theoretically predicted increase in the subpulse intensity with the carrier recovery rate of the SOA through systematic subpulse measurement. From the measured and calculated results, we conclude that our model is applicable for use in wide recovery rate range. Finally, we discuss the trade-off between the subpulses and pattern-induced intensity noise associated with the recovery rate change, which we referred to only briefly using one quick particular example in our previous letter, in a wider recovery rate range. This result illustrates that subpulse generation can be a significant limiting factor for practical DISC operations. The present modeling work will be of great help in the future development of solutions for this issue, and will also assist other researchers in modeling all-optical gate operations based on SOAs and delayed interferometers.

2. Theoretical Model of DISC-Gate Operation Based on SOA Carrier Dynamics

A DISC gate in its original concept consists of a single SOA as an optical nonlinear element, and a Mach-Zehnder interferometer (MZI), which determines the output timing window [Fig. 1(a)]. Input pulse train with a wavelength of λ_1 is combined with continuous-wave (cw) light (λ_2) and injected into the SOA. The all-optical modulation process can be modeled based on the rate equation of the excess carrier density in the SOA as

$$\frac{d}{dt} \overline{n_c(t)} = \frac{\eta_T I_{\text{OP}}}{qV} - \frac{\overline{n_c(t)}}{\tau_c} - \frac{1}{V} [G(\overline{n_c(t)}) - 1] \left[\frac{|\mathbf{E}_{\text{pulse}}(t)|^2}{h\nu_{\text{pulse}}} + \frac{|\mathbf{E}_{\text{CW}}|^2}{h\nu_{\text{CW}}} \right]. \quad (2.1)$$

Here, $\overline{n_c(t)}$ is the average $n_c(z, t)$ over the active region length. $n_c(z, t)$, the carrier density which contributes to the

*Present address: Nara Institute of Science and Technology, Ikoma, Nara 630-0192, Japan.

[†]Present address: u2t Photonics AG., Berlin 10553, Germany.

[‡]Present address: Fujitsu Access Ltd., Kawasaki 213-8586, Japan.

[§]Present address: Hitachi Communication Technology Ltd., Yokohama 244-8567, Japan.

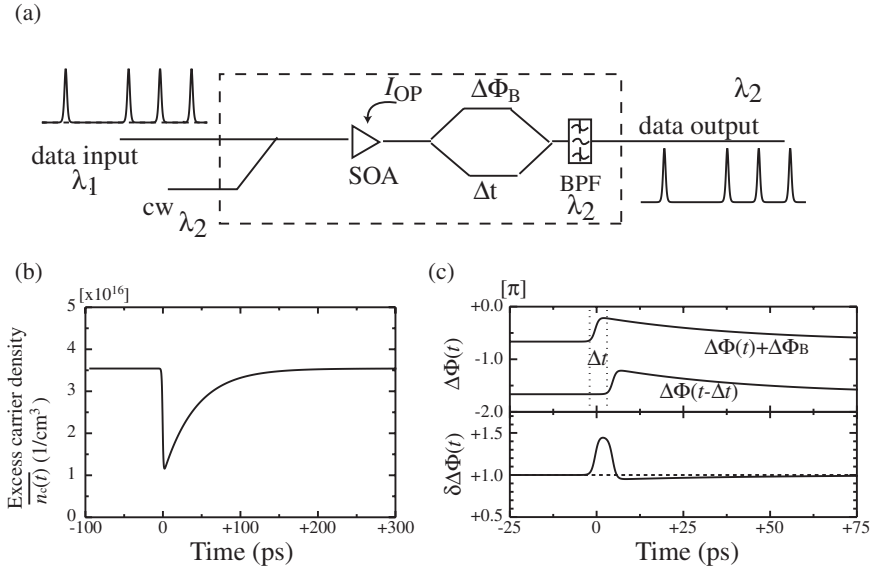


Fig. 1. Schematic and operation principles of the DISC gate: (a) Schematic of the gate. (b) Calculated example of the time profile of SOA carrier density during optical modulation. (c) Time profiles of the nonlinear phase shifts for the split optical components in the MZI, and the phase difference between them.

SOA gain, is diminished from the total carrier density, as represented by the quantum conversion efficiency η_T . I_{OP} is the injection current, τ_c is the carrier lifetime, V is the active region volume, and $\mathbf{E}_{\text{pulse}}(t)$ and \mathbf{E}_{CW} are the amplitudes of the input optical signals. The first, second, and third terms on the right-hand side of eq. (2.1) represent the carrier injection, carrier relaxation, and stimulated recombinations, respectively. $\mathbf{E}_{\text{pulse}}(t)$ for a clock operation is expressed as

$$\mathbf{E}_{\text{pulse}}(t) = \sum_m \sqrt{\frac{E_{\text{pulse}}}{2T_W}} \text{sech}\left(\frac{t - mT}{T_W}\right) \quad (2.2)$$

$(m = 1, 2, \dots, \infty),$

where E_{pulse} is the pulse energy and T_W is a parameter related to the full-width at half-maximum pulse width T_{FWHM} as

$$T_W = \frac{T_{\text{FWHM}}}{2 \ln(1 + \sqrt{2})}. \quad (2.3)$$

Since the material gain of the SOA is considered to be given by $\Gamma dg/dn \cdot n_c(z, t)$,⁹⁾ the chip gain of the SOA is expressed as

$$G(\overline{n_c(t)}) = \exp\left[\Gamma L_{\text{eff}} \frac{dg}{dn} \overline{n_c(t)}\right]. \quad (2.4)$$

Here, Γ is the confinement factor, L_{eff} is the effective length of the active region, and dg/dn is the differential gain of the active region. $n_c(t)$ decreases through stimulated recombinations as each control pulse incidents on the SOA [Fig. 1(b)], and this decrease causes an ultrafast change in the refractive index n_r of the active region through the band-filling effect. Then the co-propagating cw signal suffers nonlinear phase modulation⁹⁾ expressed as

$$\Delta\Phi(t) = -\frac{\alpha}{2} \Gamma L_{\text{eff}} \frac{dg}{dn} \overline{\Delta n_c(t)} = k_0 \Gamma L_{\text{eff}} \frac{dn_r}{dn} \overline{\Delta n_c(t)}. \quad (2.5)$$

Here, α is the linewidth enhancement factor and $k_0 = 2\pi\nu_{\text{cw}}/c$ is the wave number of the light in vacuum. The confinement factor Γ relates n_r to the effective index of the SOA. $\Delta\Phi(t)$ increases within less than one picosecond after

each pulse injection, but recovers slowly according to the effective carrier relaxation time τ_{eff} . The delayed interference scheme has been adopted to inhibit this slow response as follows: The gain-modulated and phase-modulated cw light is split into two components at the MZI, which are combined after suffering a time difference Δt and a phase difference (phase bias) $\Delta\Phi_B$ at the end of the MZI. Then the amplitude of the combined signal is expressed as

$$\mathbf{E}_{\text{out}}(t) = \frac{1}{2} \left\{ \sqrt{G(t)} \exp[i(\Delta\Phi(t) + \Delta\Phi_B)] + \sqrt{G(t - \Delta t)} \exp[i\Delta\Phi(t - \Delta t)] \right\} \mathbf{E}_{\text{cw}}, \quad (2.6)$$

and the output signal intensity $P_{\text{out}}(t)$ is expressed as

$$P_{\text{out}}(t) = |\mathbf{E}_{\text{out}}(t)|^2 = \left\{ \sqrt{G(t)G(t - \Delta t)} \cos^2[\delta\Delta\Phi(t)/2] + \frac{1}{4} \delta G(t)^2 \right\} \times |\mathbf{E}_{\text{cw}}|^2, \quad (2.7)$$

$$\delta\Delta\Phi(t) \equiv \Delta\Phi(t) - \Delta\Phi(t - \Delta t) + \Delta\Phi_B, \quad (2.8)$$

$$\delta G(t) \equiv \sqrt{G(t)} - \sqrt{G(t - \Delta t)}. \quad (2.9)$$

Thus, the output signal intensity is dominated by the phase difference $\delta\Delta\Phi(t)$. It is largely shifted from $\Delta\Phi_B$ only within $t_0 < t < t_0 + \Delta t$, where t_0 is the pulse incident time, and the output gate window is shortened to Δt [Fig. 1(c)]. Since the input data pulses at λ_1 do not pass the band-pass filter (BPF), we obtain wavelength-converted signals from the DISC gate.

There remains a problem with this scheme, however, since the recovery of $\Delta\Phi(t)$ is not linear-function-like but exponential with t , expressed as $\exp(-t/\tau_{\text{eff}})$. $d\Delta\Phi(t)/dt$ and $d\Delta\Phi(t - \Delta t)/dt$ do not balance as it is, implying that complete cancellation of the phase shift after $t > t_0 + \Delta t$ is not possible. Instead there occurs a subpulse outside the gate window, potentially causing a bit error. Note that if we can induce asymmetric phase shifts for the two components as $\phi_1 \sim \exp(-t/\tau_{\text{eff}})$ and $\phi_2 \sim f_{\text{phase}} \cdot \exp[-(t - \Delta t)/\tau_{\text{eff}}]$, we can suppress subpulse generation by selecting $f_{\text{phase}} = \exp(-\Delta t/\tau_{\text{eff}})$.⁶⁾

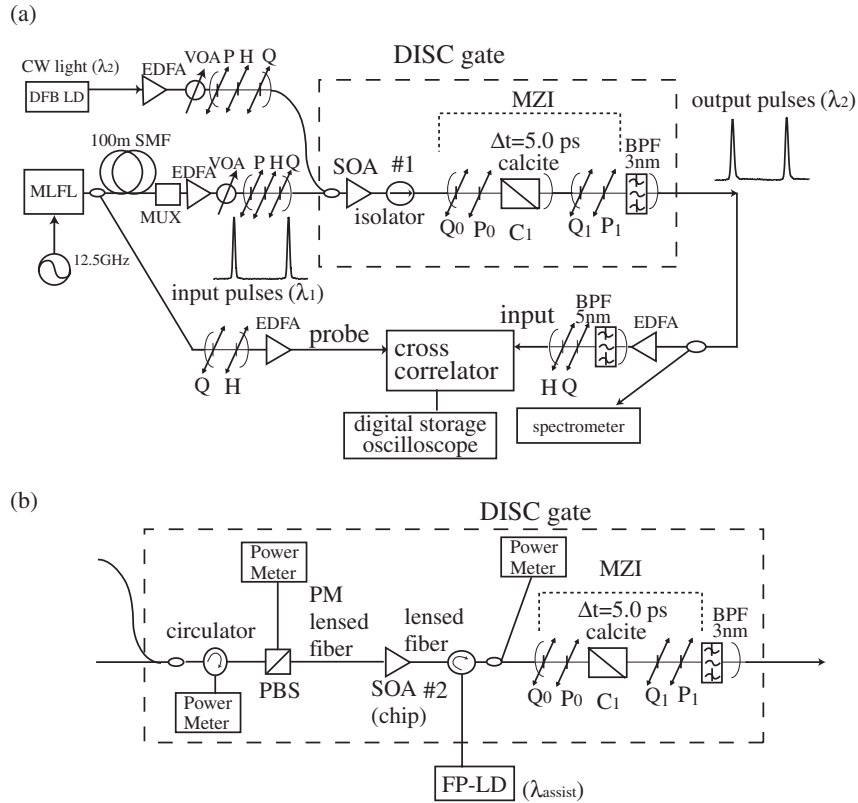


Fig. 2. Setup of the DISC-gate experiment. (a) Setup for §4.1. VOA: variable optical attenuator, MZI: Mach-Zehnder interferometer, SOA: semiconductor optical amplifier, Q: quarter-wave plate, H: half-wave plate, P: polarizer, MLFL: mode-locked fiber laser, and MUX: optical time-division multiplexer. (b) Modified DISC-gate setup for §4.2.

3. Experimental Setup for Subpulse Measurement

3.1 Overview

The generation of subpulses had not been revealed clearly before our measurement owing to the lack of monitoring resolution in previous experiments. Precise, quantitative investigation of subpulses requires waveform monitoring in a high dynamic range with a high time resolution over a long time span. Thus, we employed a cross-correlator (Femtochrome Research FR-103XR), that had a dynamic range exceeding 27 dB. Its time resolution was determined by the width of optical sampling pulses, and 2.2 ps could be achieved using pulse trains from a frequency-tunable mode-locked fiber laser (MLFL; Pritel UOC-3).

The setup for waveform monitoring in §4.1 is shown in Fig. 2(a). In this case, we used a commercially available SOA module #1 (InPhenix IPSAD1503, drive current = 250 mA) in the DISC. Some of the measured characteristics of this SOA are shown in Table I and Figs. 3(a), and 3(b). Particularly, precise characterization of the gain saturation for temporally isolated optical pulses was indispensable for the accurate subpulse calculation in §4.1. In addition, the degree of nonlinear phase shift for particular optical inputs

was estimated from the cross-phase-modulated (XPM) spectrum, as shown in Fig. 3(c),²⁾ to determine dn_r/dn later. We used a set of high-precision, high-extinction-ratio polarization-control devices Q_0 – P_1 (Optoquest) in order to construct the MZI. The rotating quarter-wave plate Q_0 and the rotating polarizer P_0 were used to adjust the polarization of the cw light to exactly 45° off the principal axis of the calcite crystal C_1 (DGD, $\Delta t = 5$ ps). The next quarter-wave plate Q_1 and rotating polarizer P_1 were used to control $\Delta\Phi_B$ precisely. Details of this polarization-based MZI will be discussed in §3.2. 25 and 12.5 GHz clock pulses were generated from the MLFL and an optical multiplexer to drive the DISC gate. The width of the pulses sent to the DISC was broadened from 2.2 to 3.8 ps with a 100-m-long single-mode fiber, to suppress carrier-heating-related phenomena inside the SOA.¹⁰⁾ The polarization of cw light from the distributed-feedback laser diode (DFB-LD) as well as the clock signal was aligned to either the transverse electric (TE) or transverse magnetic (TM) axis of the SOA at the SOA input facet, to suppress the nonlinear polarization rotation.^{11,12)}

For the measurement discussed in §4.2, where a much faster SOA was required, we used a custom-designed multiple quantum well SOA chip #2 ($L_{\text{eff}} = 1100 \mu\text{m}$), instead of the previous SOA module. The small-signal gain, the gain saturation profile, and example of the XPM spectrum are shown in Figs. 3(a), 3(b), and 3(d), respectively. The detailed properties of this SOA are also explained in ref. 13. Part of the experimental setup was modified as shown in Fig. 2(b). Signal injection to the SOA chip was achieved using a polarization-maintaining dispersion-shifted lensed fiber, with its PM axis aligned to the TE axis of the SOA. Counter-

Table I. Measured characteristics of SOA #1 used in §4.1, at $I_{\text{OP}} = 250$ mA.

Small signal gain G_0 (dB)	23
Coupling loss against pigtail fibers (dB)	2
Saturation energy for 2-ps pulse $E_{\text{pulse}}^{\text{sat}}$ (fJ)	600
Carrier lifetime τ_c (ps)	200

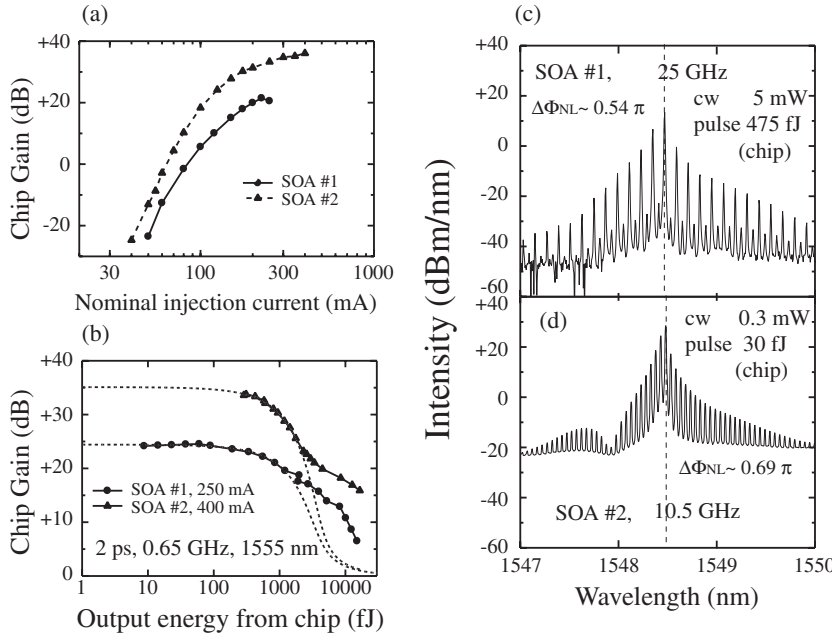


Fig. 3. Measured characteristics of SOAs. (a) Small-signal gains for cw light, $\lambda = 1548.5$ nm. (b) Gain saturation profiles for temporally isolated pulses. Dashed lines show fitting results with a theoretical function,⁹⁾ $G(E_{out}) = E_{out}/E_{pulse}^{sat} \{ \ln[\exp(E_{out}/E_{pulse}^{sat}) + G_0 - 1] - \ln G_0 \}^{-1}$. (c, d) Spectra of the cross-phase-modulated cw outputs from the SOAs. Dashed lines indicate the cw light wavelength.

propagating assist light¹⁴⁾ of $\lambda_{assist} = 1480$ nm was used in some measurements to obtain an effective recovery time as short as $\tau_{eff} = 11$ ps. The polarization-based MZI was improved so that all the components were directly connected to each other without fiber connections. This reduced the drift of the polarization-transfer property inside the MZI.

3.2 Phase bias of polarization-based MZI

As we discussed in §2, the MZI in the DISC plays a critical role in wavelength conversion and subpulse generation. Since the subpulse waveform is quite sensitive to the MZI phase bias as we will show in §4.1, precise determination of the bias value $\Delta\Phi_B$ is essential for comparison of the measured and calculated results. In this subsection,

therefore, we discuss how the set of wave plates, calcite and polarizers acts as an MZI, how we can determine $\Delta\Phi_B$ from the wave-plate settings, and the precision of $\Delta\Phi_B$.

In the first step, cw light is evenly split into two orthogonally polarized components aligned to the C_1 axes, by adjusting the Q_0 , P_0 , and C_1 angles. Seen from one of the C_1 axes, the Jones vectors of these components are expressed as

$$\mathbf{E}_{in1} = \begin{pmatrix} 1 \\ 0 \end{pmatrix}, \quad \mathbf{E}_{in2} = \begin{pmatrix} 0 \\ 1 \end{pmatrix}. \quad (3.1)$$

The Jones matrices of a calcite with an optical path length difference of Δl , a quarter-wave plate, a polarizer, and a rotation operation are expressed as

$$M_C = \begin{pmatrix} \exp\left(2\pi i \frac{\Delta l}{\lambda}\right) & 0 \\ 0 & 1 \end{pmatrix}, \quad M_Q = \begin{pmatrix} \exp\left(i\frac{\pi}{4}\right) & 0 \\ 0 & \exp\left(-i\frac{\pi}{4}\right) \end{pmatrix}, \quad (3.2)$$

$$M_P = \begin{pmatrix} 1 & 0 \\ 0 & 0 \end{pmatrix}, \quad R(\theta) = \begin{pmatrix} \cos\theta & -\sin\theta \\ \sin\theta & \cos\theta \end{pmatrix},$$

respectively.

In the MZI used in §4.1, a dispersion-shifted single-mode fiber was used to connect C_1 and Q_1 . The Jones matrix of a single-mode fiber is generally expressed by a unitary matrix¹⁵⁾ as

$$M_F = \begin{pmatrix} \cos(\theta_M) \exp(i\phi_M) & \sin(\theta_M) \exp(i\psi_M) \\ -\sin(\theta_M) \exp(-i\psi_M) & \cos(\theta_M) \exp(-i\phi_M) \end{pmatrix}, \quad (3.3)$$

where θ_M , ϕ_M , and ψ_M are parameters to be measured separately.

Thus, the two components \mathbf{E}_{in1} and \mathbf{E}_{in2} are converted to

$$\begin{aligned} \mathbf{E}_{out1} &= M_P R[-(\theta_{P_1} - \theta_{Q_1})] M_Q R(-\theta_{Q_1}) M_F R(\theta_{C_1}) M_C \mathbf{E}_{in1}, \\ \mathbf{E}_{out2} &= M_P R[-(\theta_{P_1} - \theta_{Q_1})] M_Q R(-\theta_{Q_1}) M_F R(\theta_{C_1}) M_C \mathbf{E}_{in2}, \end{aligned} \quad (3.4)$$

where θ_{C_1} , θ_{Q_1} , and θ_{P_1} are the angles of the corresponding devices' axes. Then the complex ratio of these parallel vectors determines $\Delta\Phi_B(\theta_{Q_1}, \theta_{P_1})$ and the mixing ratio $r(\theta_{Q_1}, \theta_{P_1})$ as

$$\mathbf{E}_{out2} = \mathbf{E}_{out1} \times r \exp(i\Delta\Phi_B). \quad (3.5)$$

The output signal of the MZI is given by $\mathbf{E}_{out} = \mathbf{E}_{out1} + \mathbf{E}_{out2}$. \mathbf{E}_{out} becomes zero when $r = 1$ and $\Delta\Phi_B = \pi$. This can be achieved by adjusting θ_{Q_1} and θ_{P_1} properly, so that Q_1 eliminates the ellipticity of the combined signal and P_1 extinguishes its outcome. Slight detunings of θ_{Q_1} and θ_{P_1} from these conditions lead to a shift in $\Delta\Phi_B$. Figure 4 shows the calculated dependence of $\Delta\Phi_B$ for the MZI used in §4.1 on $\Delta\theta_{Q_1}$, while keeping $\Delta\theta_{P_1} - \Delta\theta_{Q_1}$ constant ($\Delta l/\lambda = -973.392$, $\theta_{C_1} = 68^\circ$, $\theta_M \sim 0.85$ rad, $\phi_M \sim 1.98$ rad,

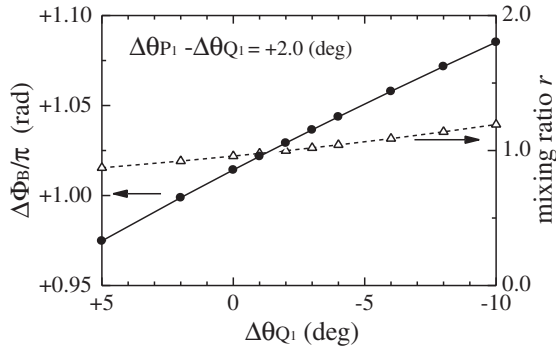


Fig. 4. Calculated dependences of MZI-bias (solid) and mixing ratio (dashed) on quarter-wave plate angle.

$\psi_M \sim 2.76$ rad, $\theta_{Q_1} \sim 131^\circ + \Delta\theta_{Q_1}$, $\theta_{P_1} \sim -64.5^\circ + \Delta\theta_{P_1}$. $\Delta\theta_{P_1} - \Delta\theta_{Q_1}$ was kept constant as an approximate means of reducing r shift, and it was shifted from 0 to $+2^\circ$ in order to slightly compensate for the r shift at around $\Delta\theta_{Q_1} = -3$ to -6° . Then $\Delta\Phi_B$ shifts linearly with $\Delta\theta_{Q_1}$, and $d\Delta\Phi_B/d\Delta\theta_{Q_1} = -7.3 \times 10^{-3}\pi$ (rad/deg). Thus, we could accurately control $\Delta\Phi_B$ ($\sim \pm 0.004\pi$ rad) through precise ($\sim \pm 0.5^\circ$) adjustments of wave-plate angles. Here we note that the actual fiber transfer matrix M_F slightly drifted with time. To compensate for this issue, we periodically adjusted θ_{Q_1} and θ_{P_1} to angles where $\Delta\Phi_B$ became π in the case in §4.1, and carefully compensated for the angle drifts.

4. Results

4.1 Subpulse measurement and calculation with systematic MZI-bias shifts

In this subsection, we review our first observation of subpulses reported in ref. 8. First, we operated the DISC at 25-GHz operation frequency, with clock pulse input (+12.3 dBm, $\lambda_1 = 1560$ nm) and cw input (+9 dBm, $\lambda_2 = 1548.5$ nm) into the SOA module #1, and observed its output

waveform. Figure 5(a) shows a typical cross-correlation trace of the DISC output that we measured after maximizing the extinction ratio by adjusting Q_1 and P_1 . As shown in Fig. 5(a), the extinction ratio was limited to 25 dB by small subpulse-like components between the output pulses. Then, to observe the waveform of the remaining components in more detail, we dropped the pulse frequency from 25 to 12.5 GHz and carefully optimized the wave-plate angles once again. The average power of the 12.5 GHz pulse train was +13.5 dBm. At this frequency, the extinction ratio was limited to about 18 dB by several types of relatively large subpulse-like components depending on the Q_1 and P_1 settings [Figs. 5(b)–5(d)].

After that, we calculated the DISC output waveform to demonstrate that the above subpulse-like components actually result from the operating principle modeled in §2. First, we chose the parameter values for use in the simulation, taking measured chip gain, saturation energy, and the recovery time of the SOA into account (Table I). The saturation energy was changed to 600 fJ from that used in our previous report⁸⁾ (1080 fJ). The new value was obtained from the precise measurement of gain saturation energy for temporally isolated ultrafast pulses [Fig. 3(b)], while the former value was estimated indirectly from a measured result of gain saturation for a 25 GHz pulse train and using numerical simulation. dn_r/dn was chosen so that the degree of the nonlinear phase shift in the 25 GHz operation becomes 0.5π [Fig. 3(c)]. The chosen parameter values are summarized in Tables II and III. Then we calculated output waveforms using eqs. (2.1)–(2.9). We could obtain subpulse waveforms quite similar to the measured data, as shown in Figs. 6(a)–6(d), after choosing $\Delta\Phi_B$ values properly. The calculated relative peak intensities of the subpulses were -24 dB in Fig. 6(a) and -18 dB in Fig. 6(b). Note that the calculated subpulse intensities increased by approximately 2 dB than before, and approached the measured values. This was due to the more suitable choice of SOA parameters as discussed previously. Also,

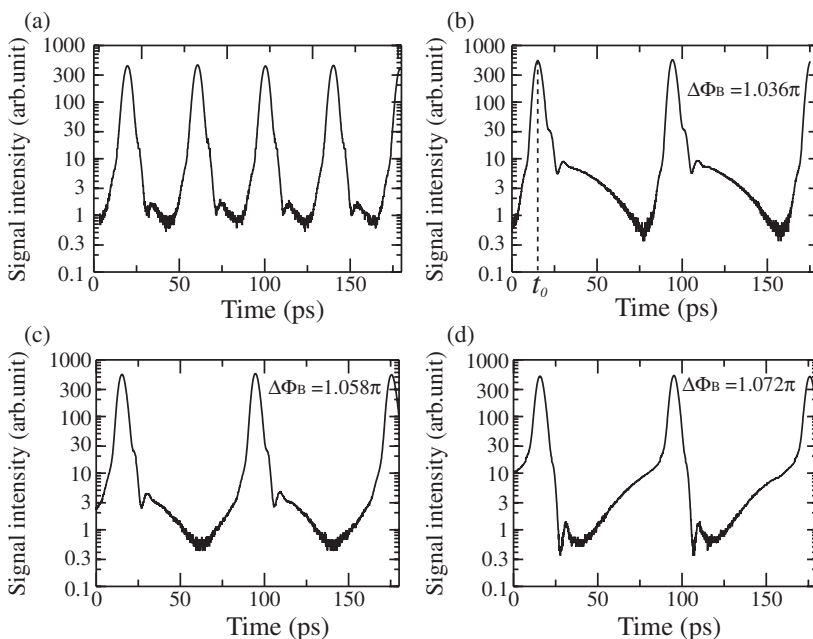


Fig. 5. Measured cross-correlation traces of the DISC output with different Q_1 and P_1 settings: (a) with +12.3-dBm, 25-GHz input pulses, (b)–(d) with +13.5-dBm, 12.5-GHz input pulses [(b) $\Delta\theta_{Q_1} = -3^\circ$, $\Delta\theta_{P_1} = -1^\circ$, (c) $\Delta\theta_{Q_1} = -6^\circ$, $\Delta\theta_{P_1} = -4^\circ$, (d) $\Delta\theta_{Q_1} = -8^\circ$, $\Delta\theta_{P_1} = -6^\circ$]. Calculated phase biases are shown in each graph.

Table II. Parameters used in the DISC-gate simulation.

	Fig. 6(a)	Figs. 6(b)–6(d)	§4.2
Pulse repetition frequency f (GHz)	25	12.5	10.5 (50)
Input pulse width (FWHM) T_{FWHM} (ps)	3.8	3.8	2.0
Input pulse energy (into chip) E_{pulse} (fJ)	429	1129	30
Input cw power (into chip) P_{cw} (mW)	5	5	0.3
Delay time in the MZI Δt (ps)	5.0	5.0	5.0
Correlator probe width T_{probe} (ps)	2.2	2.2	2.0
Frequency of cw light ν_{cw} (THz)	193.7	193.7	193.7
Frequency of pulsed light ν_{pulse} (THz)	192.1	192.1	192.8

Table III. SOA fundamental parameters used in the calculation, and derived quantities.

	§4.1	§4.2
Injection current I_{OP} (mA)	250	$400 \times a$
Active region length (effective) L_{eff} (μm)	700	1100
Active region volume V (cm^3)	1.4×10^{-10}	5.2×10^{-11}
Confinement factor Γ	0.2	0.2
SOA carrier lifetime τ_c (ps)	200	$35/a$
SOA differential gain dg/dn (cm^2)	2.17×10^{-15}	6.36×10^{-16}
Carrier-conversion efficiency η_T	0.079	0.34
refractive index change dn_i/dn (cm^3)	-1.87×10^{-19}	-1.4×10^{-20}
Maximum-available carrier density \bar{n}_c^{max} (cm^{-3})	1.76×10^{17}	5.72×10^{17}
SOA small-signal gain G_0 (dB)	23.4	34.8
Saturation energy for pulse $E_{\text{pulse}}^{\text{sat}}$ (fJ)	600	473
Phase shift at complete carrier depletion $\Delta\Phi_{\text{max}}$	$+6.0\pi$	$+2.3\pi$

$\Delta\Phi_B$ values in Figs. 5(b), 5(c), 6(b), and 6(c) showed improved matchings.

The behavior of relative intensities of subpulse-like components as functions of the phase bias $\Delta\Phi_B$ is shown

in Fig. 7. The relative intensity was taken at three time positions ($t = t_0 + 15$ ps, $t_0 + 40$ ps, and $t_0 + 65$ ps, where t_0 is the primary pulse's position). The calculated behavior was quite similar to the measured data, taking the ~ 27 -dB dynamic range of the cross-correlator into account. The mismatch in the intensity was small, 1 to 2 dB for $t = t_0 + 15$ ps series, at $\Delta\Phi_B = 1.00\pi$ to 1.08π . We are aware that the phase-bias dependence and extinction ratios are dominated by many parameters, and future improvement in the gate model may solve the remaining small mismatch. Regarding subpulse intensity, we consider that the gate model in this paper provides the most reliable predictions currently available.

Thus, as shown in Figs. 5–7, we observed a good match between the measured and calculated waveforms and the phase-bias dependence. Therefore, we presume that our subpulse generation model has been experimentally verified for a particular recovery rate, and that we can predict subpulse intensity with 1 to 2 dB accuracy using this model.

4.2 Trade-off regarding subpulse generation and pattern-induced intensity noise

The subpulse intensity of the DISC output discussed in §4.1 could be suppressed by tuning the MZI bias down to ~ -20 dB, which is negligible for practical applications. Nevertheless, we have regarded subpulse generation as a major issue in the case of random-data operation, because of the trade-off relationship between subpulse generation and pattern-induced intensity noise. If the input signal is not a continuous clock but has a random pattern, the instantaneous carrier density in the SOA varies upon each signal injection depending on the preceding input-signal pattern. Then the intensities of the output signals become pattern-dependent. This effect can be reduced by accelerating the carrier recovery with current injection or assist light injection. Our subpulse model indicates, however, that a subpulse becomes large as we increase carrier recovery rate. In this subsection, we will discuss the measured and calculated results for this effect.

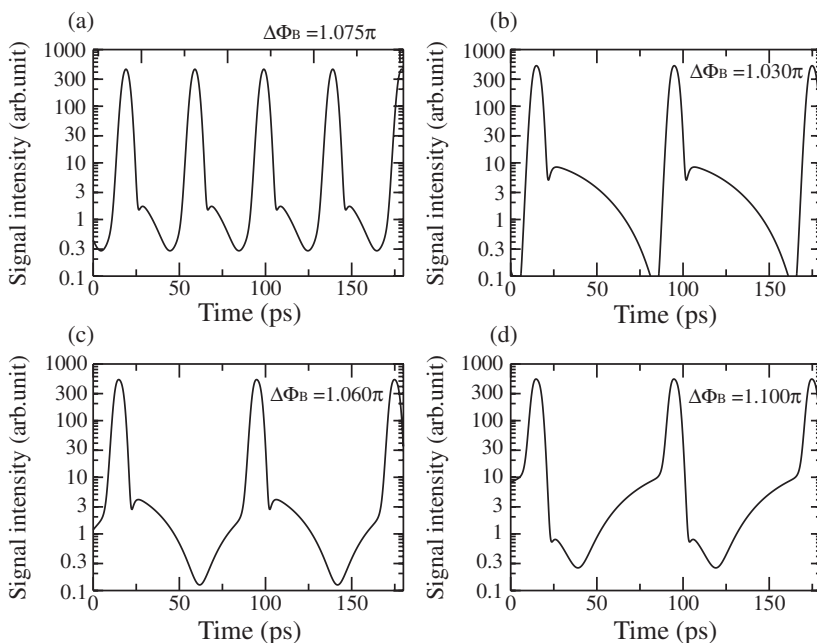


Fig. 6. Calculated cross-correlation traces of the DISC output: (a) with 25-GHz input pulses, (b)–(d) with 12.5-GHz pulses [(b) $\Delta\Phi_B = 1.030\pi$, (c) $\Delta\Phi_B = 1.060\pi$, (d) $\Delta\Phi_B = 1.100\pi$]. Other parameter values are summarized in Tables II and III.

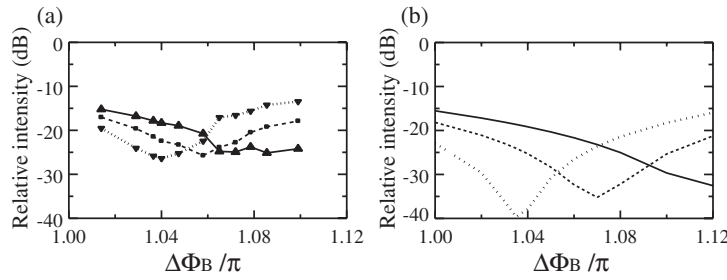


Fig. 7. Relative intensities of the subpulse-like components in 12.5-GHz DISC output: (a) from experimental results; (b) from calculations. These were obtained at three time positions: $t = t_0 + 15$ ps (solid), $t_0 + 40$ ps (dashed), and $t_0 + 65$ ps (dotted).

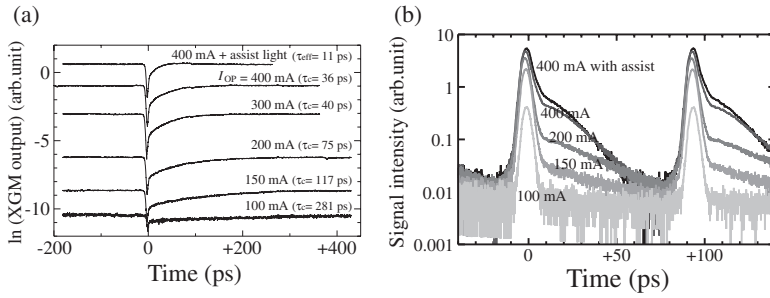


Fig. 8. DISC output waveforms for several carrier recovery rates. (a) XGM profiles of SOA #2 for several operation currents, indicating the recovery acceleration. The cw-probe intensity and pulse energy injected into the chip were set at -25 dBm and 10 fJ, respectively. Note that each plot is translated intentionally in vertical direction. (b) 10.5 -GHz DISC output waveforms. $\Delta\Phi_B$ was set to be 1.0π .

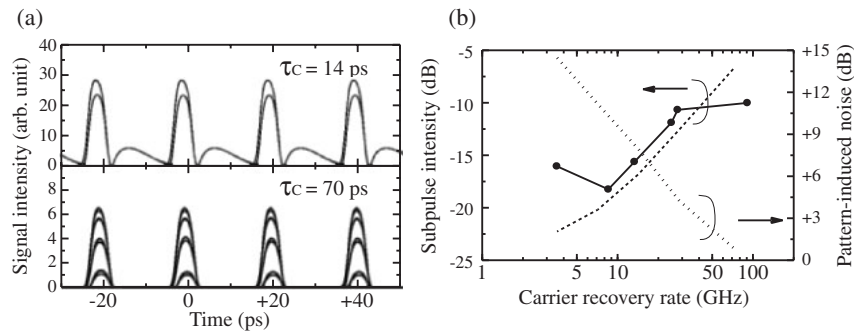


Fig. 9. Trade-off between pattern-dependent intensity noise and subpulse noise. (a) Calculated eye diagrams of the DISC output for 50 Gbps pseudo-random signal, for two carrier recovery rates. The cross-correlation process was omitted for simplicity. Parameter values are summarized in Tables II and III. (b) Measured (solid) and calculated (dashed) subpulse intensities against the carrier recovery rate $1/\tau_c$ at 10.5 GHz, and calculated pattern-induced noise for the 50 Gbps signal (dotted).

We systematically measured subpulse waveforms for several carrier lifetimes, using the customized SOA chip #2, as explained in §3.1. Figure 8(a) shows the gain-recovery profiles of the SOA for several injection currents, measured with the cross-correlator.¹³⁾ The recovery time τ_c was reduced from 280 to 36 ps as we increased the injection current I_{OP} from 100 to 400 mA, and it was approximately inversely proportional to I_{OP} above 150 mA. The effective recovery time τ_{eff} was further shortened to 11 ps after we injected 80 mW assist light with a nearly transparent wavelength (1480 nm) into the chip. Using this SOA, we measured the DISC output waveforms on each I_{OP} . The operation frequency was 10.5 GHz. The input pulse width, wavelength, and energy into the chip were 2 ps, 1555 nm and 30 fJ, respectively. The cw light wavelength and power into the chip were 1548.5 nm and -5 dBm, respectively. The delay time of the MZI was set to 5 ps. The MZI phase bias was fixed at 1.0π throughout the measurement, since the optimum phase bias depends largely on τ_c (τ_{eff}). The measured waveforms are shown in Fig. 8(b). We found that the relative intensity of the subpulse increased up to -10 dB,

as we increased the carrier recovery rate $1/\tau_c$ [Fig. 9(b)]. The measured subpulse intensity for $\tau_c = 280$ ps seems less accurate owing to the low output power and S/N ratio.

Meanwhile, we could predict this result qualitatively using our gate model. For simplicity, we assumed that τ_c was inversely proportional to I_{OP} , and that other fundamental parameters did not change with I_{OP} . The adopted values are summarized in Tables II and III. The values in Table III were determined in view of measured characteristics of SOA #2 at $I_{OP} = 400$ mA [Figs. 3(a), 3(b), 3(d), and 8(a)]. Then the measured and calculated subpulse intensities agreed quite well for most $1/\tau_c$ values [(Fig. 9(b)]. We regarded this matching as convincing evidence that our model is applicable in a wide $1/\tau_c$ range. Some discrepancy at $\tau_c = 11$ ps probably originates from the difference between the acceleration mechanism with current injection and that with assist-light injection. This result clearly indicates that we can suppress subpulse generation as long as we keep the carrier recovery rate small.

As we mentioned above, this method of subpulse suppression leads to an increase in pattern-induced intensity

noise. We calculated the DISC output waveforms for a 50 Gbps input pulse train with a pseudorandom bit sequence (pattern length = $2^{15} - 1$), and calculated the pattern-induced noise from the intensity ratio of the largest and smallest signals in the output pulse train [Fig. 9(a)]. The values of the other parameters remained unchanged from the former calculations. The dotted line in Fig. 9(b) shows the dependence of the pattern-induced noise on recovery rate. Evidently, this pattern-induced noise can be suppressed by increasing recovery rate, which leads to the unwanted increase in subpulse intensity.

In this way, our model shows the trade-off between subpulse generation and the pattern-induced noise. Although what we have shown is only a particular example, we consider that this trade-off relation arises fairly universally. We will encounter subpulses as large as -7 dB, in the present case for example, as we suppress the pattern-induced noise down to 1 dB. The situation may become even worse depending on other operating conditions such as signal bit rate, signal duty ratio, and control pulse energy. Therefore, we consider that a new gating scheme for resolving this issue is necessary. Regarding the past wavelength conversions at 160³⁾ and 320 GHz,⁵⁾ we speculate that additional phenomena such as nonlinear polarization rotation and carrier heating in the SOA contributed to unexpected suppression of subpulse generation.⁶⁾ Also, employing a blue-shifted optical filter in the latter case is considered advantageous in reducing pattern-induced noise¹⁶⁾ at the cost of output signal power and system simplicity. We consider that subpulse generation should be one of the major design features for DISC-type wavelength converters and should be evaluated using the current model or an expanded model in the near future.

5. Conclusions

We have studied subpulse generation in the wavelength-converted signal from a DISC gate operated at 10 to 25 GHz, both theoretically and experimentally. We described our subpulse generation model and experimental method in detail, and reviewed our first observations of subpulse generation described in our previous letter. As good matching as 1 to 2 dB was obtained between the measured and calculated subpulse intensities. The dependence of subpulse waveforms on the MZI phase bias was well explained at around $\Delta\Phi_B = 1.00\pi$ to 1.08π .

In addition to these results, we demonstrated that our model is applicable in a wide range of SOA carrier recovery rates. The impact of carrier-recovery acceleration (from $\tau_c = 280$ ps to $\tau_{\text{eff}} = 11$ ps) on subpulse waveforms was systematically studied using a DISC with a customized SOA chip. We obtained good agreement between the measured and calculated subpulse intensities for the majority of the recovery rate range.

Using our subpulse model, we discussed the trade-off between subpulse generation and pattern-induced intensity noise. Our calculations indicated that significant subpulses may emerge when we suppress pattern-induced intensity noise, which may lead to difficulty in the practical high-speed operation of the DISC. This result suggests that part of the DISC structure should be improved to overcome this trade-off. We are in the process of solving this problem using new gating schemes, for example, using an expanded DISC including an optical spectral synthesizer.¹⁷⁾ We believe that success in such modeling will be valuable not only for the practical applications of the DISC but also for the detailed understanding of other kinds of all-optical gates using SOAs, delayed interferometers, and so on.

Acknowledgements

This research work was supported by research project grant #B15360027, "Optical logic gates in the sub-terahertz frequency region", of the Ministry of Education, Culture, Sports, Science, and Technology (MEXT) and the research project grant, "Ultra-low-power and ultrafast optical memory/switching device", of the New Energy and Industrial Technology Development Organization (NEDO), and the 21st-Century University's Center of Excellence (COE) program, "Innovation in coherent optical science", of the University of Electro-Communications, Japan.

- 1) K. E. Stubkjaer: *IEEE J. Sel. Top. Quantum Electron.* **6** (2000) 1428.
- 2) Y. Ueno, S. Nakamura, and K. Tajima: *J. Opt. Soc. Am. B* **19** (2002) 2573.
- 3) S. Nakamura, Y. Ueno, and K. Tajima: *IEEE Photonics Technol. Lett.* **13** (2001) 1091.
- 4) J. Leuthold, G. Raybon, Y. Su, R. Essiambre, S. Cabot, J. Jaques, and M. Kauer: *Electron. Lett.* **38** (2002) 890.
- 5) Y. Liu, E. Tangdiongga, Z. Li, H. de Waardt, A. M. J. Koonen, G. D. Khoe, X. Shu, I. Bennion, and H. J. S. Dorren: *J. Lightwave Technol.* **25** (2007) 103.
- 6) Y. Ueno: *Jpn. J. Appl. Phys.* **43** (2004) L665.
- 7) M. L. Nielsen and J. Mørk: *J. Opt. Soc. Am. B* **21** (2004) 1606.
- 8) J. Sakaguchi, M. L. Nielsen, T. Ohira, R. Suzuki, and Y. Ueno: *Jpn. J. Appl. Phys.* **44** (2005) L1358.
- 9) G. P. Agrawal and N. A. Olsson: *IEEE J. Quantum Electron.* **25** (1989) 2297.
- 10) J. Mørk and A. Mecozzi: *J. Opt. Soc. Am. B* **13** (1996) 1803.
- 11) H. Soto, D. Erasme, and G. Guekos: *IEEE Photonics Technol. Lett.* **11** (1999) 970.
- 12) R. J. Manning, A. Antonopoulos, R. Le Roux, and A. E. Kelly: *Electron. Lett.* **37** (2001) 229.
- 13) J. Sakaguchi, F. Salleras, K. Nishimura, and Y. Ueno: *Opt. Express* **15** (2007) 14887.
- 14) M. A. Dupertuis, J. L. Pleumeekers, T. P. Hessler, P. E. Selbmann, B. Deveaud, B. Dagens, and J. Y. Emery: *IEEE Photonics Technol. Lett.* **12** (2000) 1453.
- 15) G. D. VanWiggeren and R. Roy: *Appl. Opt.* **38** (1999) 3888.
- 16) M. L. Nielsen, J. Mørk, J. Sakaguchi, R. Suzuki, and Y. Ueno: presented at Optical Fiber Communication Conf., 2005, OThE7.
- 17) Y. Ueno, R. Nakamoto, J. Sakaguchi, and R. Suzuki: *Opt. Express* **14** (2006) 12655.